

Experimental and Numerical Studies of Spontaneous Imbibition with Different Boundary Conditions: Case Studies of Middle Bakken and Berea Cores

[†]Department of Petroleum Engineering and [‡]Department of Chemistry, University of North Dakota, Grand Forks, North Dakota 58202, United States

ABSTRACT: Tight oil and gas are becoming increasingly important energy sources in North America. Spontaneous imbibition is an important mechanism in oil and gas recovery from tight reservoirs. In this study, countercurrent spontaneous imbibition experiments and nuclear magnetic resonance (NMR) were combined to study the imbibition and the fluid distribution in eight core samples. NMR is able to detect fluid distribution in different sizes of pores ranging from micropores to fractures. Before the experiments, Middle Bakken and Berea cores were saturated with air. Then imbibition experiments with one end open (OEO) and two ends closed (TEC) boundary conditions were carried out. The numerical solutions of spontaneous imbibition models were matched with experimental results by choosing reasonable parameters. The capillary pressure and relative permeability were obtained from the matching. Moreover, the gravity effect on the spontaneous imbibition was analyzed. It was found that the gravity can be neglected for tight rocks. However, it has significant impacts on high-permeability rocks. The recovery factor of OEO imbibition exhibits a linear relationship with \sqrt{t} . However, the TEC imbibition shows a poor linear relationship with \sqrt{t} at the late stage. This research provides new methods to obtain capillary pressure and relative permeability from spontaneous imbibition experiments with OEO and TEC boundary conditions and advances crucial mechanisms for the development of tight reservoirs.

1. INTRODUCTION

In fractured reservoirs, imbibition is an important process to improve oil and gas recovery from the matrix. 1,2 The spontaneous imbibition mechanisms in rock and coal are key issues that need to be focused upon to improve recovery in the development of the tight oil, 3,4 shale and tight gas, 5-7 coalbed methane. 8,9 Spontaneous imbibition is the process of a wetting phase displacing a non-wetting phase in a porous media in the presence of capillary pressure. Depending upon the flow directions of wetting and non-wetting phases, spontaneous imbibition can be divided into cocurrent imbibition and countercurrent imbibition. Assuming that a rock sample is water-wet, cocurrent imbibition occurs when the water and oil flow in the same direction through the inlet, whereas countercurrent imbibition occurs as the water and oil flow in opposite directions. 10,11 Some experiments and numerical studies show that the recovery rate and displacement efficiency of cocurrent imbibition are much higher than those of countercurrent imbibition. 12,13 However, countercurrent spontaneous imbibition is normally regarded as the dominant imbibition mechanism in fractured reservoirs. 14-16

For countercurrent spontaneous imbibition, a presaturated core plug is submerged in water. Depending upon boundary conditions of the core plug, there are several kinds of countercurrent spontaneous imbibition: (1) all faces open (AFO), (2) two ends closed (TEC), (3) two ends open (TEO), and (4) one end open (OEO). The schematic of four kinds of spontaneous imbibition is presented in Figure 1. Boundary conditions have great impacts on imbibition performances. AFO is a commonly used method in spontaneous imbibition experiments because it is the easiest to conduct and has the

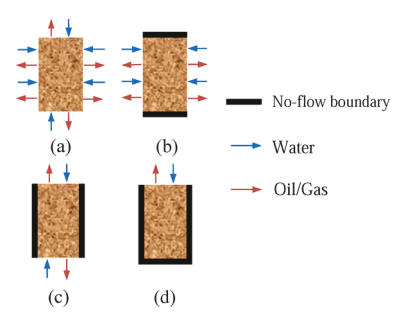


Figure 1. Schematic of four boundary conditions: (a) all faces open (AFO); (b) two ends closed (TEC); (c) two ends open (TEO); (d) one end open (OEO).

highest recovery rate. 18,19 However, the flow patterns of the AFO boundary condition are complicated due to the coexistence of cocurrent and countercurrent flow through the inlets. 18 Therefore, the established mathematical models cannot be applied to AFO imbibition.²⁰ Boundary conditions will impact the contact surface between the core and water and have significant effects on the recovery rate. Cheng et al. 21 and Lyu et al. 19 demonstrated that the AFO imbibition has the highest recovery rate and TEO has the lowest recovery rate. However, boundary conditions have a negligible impact on the ultimate recovery factor. ^{17,22} In addition, other factors, such as permeability, relative permeability, capillary pressure, initial

Received: March 24, 2019 Revised: May 15, 2019 Published: May 23, 2019

Table 1. Mineralogical Composition of Berea and Bakken Samples

samples	kaolonite (wt %)	illite (wt %)	chlorite (wt %)	quartz (wt %)	calcite (wt %)	dolomite (wt %)	feldspar (wt %)	pyrite (wt %)	halite (wt %)
Berea cores	5			88		2	5		
Bakken1		9	3	39	10	22	15	1	1
Bakken2									
Bakken3		11	4	38	14	15	15	2	1
Bakken4									

water saturation, fluid viscosity, interfacial tension, and wettability, also have effects on the imbibition process.^{20,23–27}

Spontaneous imbibition is usually modeled by a set of differential equations. The solutions of those equations require functions of capillary pressure and relative permeability to the wetting phase and non-wetting phase. Matching of a mathematical model with the experimental results is a new method to obtain relative permeability and capillary pressure. Li et al.²⁸ performed spontaneous imbibition simulation with the OEO boundary condition. They derived a mathematical model without considering the gravity effect. Then the brine/air capillary pressure and relative permeability were obtained by matching the model with experiments. Schmid et al.²⁹ derived a set of semianalytical solutions for one-dimensional imbibition. In order to derive the analytical solutions, the water front position was obtained experimentally as a function of the square root of time. Alyafei et al.³⁰ and Schmid et al.³¹ derived a closed form of analytical solutions for spontaneous imbibition based on the fractional flow theory. Mathematical models are important in order to understand the mechanisms of spontaneous imbibition. Haugen et al.¹⁴ proposed models to scale relative permeability and capillary pressure for imbibition of cores with TEC and OEO boundary conditions. Alyafei and Blunt¹¹ conducted onedimensional water cocurrent imbibition on sandstones and obtained the relative permeability and capillary pressure. While there have been various models focusing on linear imbibition, there are very few research studies about modeling imbibition with complex boundary conditions such as TEC and AFO. Besides, the gravity effects on spontaneous imbibition have not been well studied.

Recently, low-field nuclear magnetic resonance (NMR) techniques have been introduced to analyze the spontaneous imbibition to observe fluid distribution and core petrophysical properties. NMR transverse relaxation time (T_2) of the saturated cores can be converted into pore size distribution, porosity, and fluid distribution at the pore scale. 19,32,33 Liang et al. 34 used NMR T_2 to monitor the oil saturation changes behind the spontaneous imbibition front. Their results indicated that the smaller the average pore size, the more rapid the saturation changes behind the imbibition front. Cheng et al.²¹ investigated the residual oil distribution for oil/water displacement using spontaneous imbibition combined with NMR and MRI technologies. Their results demonstrated that oil in micropores is preferentially expelled by water due to high capillary pressure. Another important implication of NMR is to detect the movable fluid distribution. Lyu et al.35 studied the movable water distribution in tight rocks using the centrifugal method. Their results show that the movable fluid is controlled by pore size and the connectivity between pores. Gao and Li³⁶ measured movable fluid percentages for different cores and concluded that the movable fluid percentage goes higher as the permeability increases. NMR provides a fast and nondestructive

technique and has become a common experimental method in imbibition interpretation and analysis of core properties.

In this work, we experimentally and numerically explored the spontaneous imbibition with OEO and TEC boundary conditions. Accurate experiments of brine imbibing into air-filled cores were carried out with continuous recording of mass changes using a high-precision balance. The pore size distribution and fluid distribution in cores were obtained from the NMR method. Furthermore, new methods to determine capillary force and relative permeability were proposed by matching mathematical models with spontaneous imbibition experiments with OEO and TEC boundary conditions.

2. EXPERIMENTAL PROCEDURES

2.1. Rocks and Fluids. Eight core plugs were selected to conduct spontaneous imbibition experiments. Four Bakken cores were obtained from the Middle Member of the Bakken Formation in North Dakota, USA. Four Berea cores were cut from outcrops in Cleveland Quarries, Ohio, USA. All of those core plugs were drilled perpendicular to bedding. The mineralogical analysis using X-ray diffraction (XRD) was conducted for the core samples and is shown in Table 1.

As indicated in Table 1, the dominant mineral of Berea cores is quartz. However, the major minerals of the Middle Bakken samples are quartz, dolomite, feldspar, and calcite. Middle Bakken cores are light gray limestone. Berea cores are fine-grained, clay-cemented quartz sandstone. Core sample preparation includes extracting cores with toluene and ethanol and drying core samples in an oven at 105 °C. After the cleaning and drying of core samples, routine analysis such as measuring mass, diameter length, helium porosity, and helium permeability was performed. The petrophysical properties of those samples are presented in Table 2.

Table 2. Summary of the Petrophysical Properties of Core Plugs

samples	diameter (cm)	length (cm)	permeability (mD)	porosity (%)
Bakken1	3.78	2.12	0.49	8.4
Bakken2	3.79	3.15	7.80	5.1
Bakken3	3.78	1.86	8.00	3.6
Bakken4	3.77	4.29	0.13	4.9
Berea1	3.94	5.08	99.8	22.1
Berea2	3.90	4.91	80.4	23.4
Berea3	3.95	4.55	10.7	23.1
Berea4	3.96	4.61	61.2	23.8

As shown in Table 2, Middle Bakken samples are tight rocks and have lower porosity and permeability than Berea samples. All experiments were conducted at ambient conditions: $23\,^{\circ}\text{C}$ and atmospheric pressure (100 KPa). The brine solution consisted of 1 wt % NaCl and 1 wt % KCl to prevent the swelling problem. The density of brine was $1.011\,\text{g/cm}^3$, and its viscosity was $0.896\,\text{mPa·s.}^{37}$ The air density was $0.0012\,\text{g/cm}^3$, and its viscosity was $0.018\,\text{mPa·s.}^{38}$.

2.2. Imbibition Experiments. The schematic of the experimental apparatus is presented in Figure 2. The masses of core samples were continuously recorded using a high-precision balance with 0.001 g

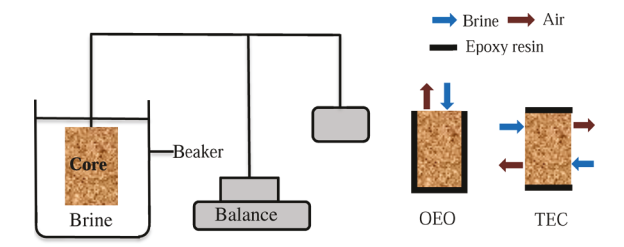


Figure 2. Schematic of the experimental setup.

accuracy. Archimedes' principle shows that the magnitude of the buoyant force in the core plug is equal to the weight of the brine it displaces, which is a constant. It can be verified that the increase of the mass equals the mass of the brine that is imbibed into the core minus the mass of the air displaced out of the core. Two sets of experiments with different boundary conditions were carried out. In the first set, one end open (OEO) spontaneous imbibition experiments were conducted on core plugs Bakken1, Bakken4, Berea3, and Berea4. In the second set, two ends closed (TEC) imbibition experiments were performed on cores Bakken2, Bakken3, Berea1, and Berea2. To ensure that only countercurrent imbibition occurred, core plugs were sealed with epoxy resin. For OEO imbibition, the bottom face and cylindrical surface were sealed with epoxy resin. For TEC imbibition, the top and bottom faces of cores were sealed with epoxy resin.

2.3. NMR Experiments. The nuclear magnetic resonance (NMR) tests for cores at fully brine-saturated conditions (or preimbibition) and after imbibition conditions were carried out. The experiments include the following steps: (1) A ZYB-II Vacuum Saturation Device was used to vacuum the cores for 24 h and then saturate cores with brine at 20 MPa for 7 days. Then the masses of the cores were measured. (2) Raw NMR data of 100% brine-saturated cores were measured. (3) The cores were dried in an oven at 105 °C. (4) Brine imbibition experiments with different boundary conditions were performed. (5) NMR T2 distributions of Berea and Bakken samples were measured as imbibition experiments completed. NMR measurements were carried out with low-field (2 MHz) NMR equipment (Oxford Instruments Geospec2 Rock Core Analyzer). NMR measurements were conducted with an inbuilt Oxford Instruments pre-emphasis testing EDDYCM pulse sequence.³⁹ The NMR measurement parameters for Bakken samples were as follows: 150 ms waiting time, 4600 number of echoes, 200 μ s echo time, and 64 number of scans. The NMR measurement parameters for Berea samples were as follows: 1500 ms waiting time, 66700 number of echoes, 100 μ s echo time, and 64 number of scans. The laboratory temperature and magnet temperature of the NMR spectrometer were 23 and 20 °C, respectively.

3. IMBIBITION MODELS

3.1. OEO Spontaneous Imbibition. Countercurrent imbibition with OEO boundary conditions is a one-dimensional flow. Although air is compressible, the experiments were conducted at atmospheric pressure. The air is compressed at the short initial period of spontaneous imbibition.²⁸ The pressure change in the air phase is negligible, with little or no air volume change.³⁰ Thus, incompressible flow in a homogeneous porous media is assumed. The wetting phase (water) conservation equation can be written as

$$\frac{\partial v_{\rm w}}{\partial x} = -\phi \frac{\partial S_{\rm w}}{\partial t} \tag{1}$$

Considering the experimental setup in this paper, gravity is regarded as the driving force. The Darcy velocity of the wetting phase is

$$v_{\rm w} = \frac{kk_{\rm rw}}{\mu_{\rm w}} \left(-\frac{\partial P_{\rm w}}{\partial x} + g\rho_{\rm w} \right) \tag{2}$$

The Darcy velocity of the non-wetting phase (air) is

$$v_{\rm g} = \frac{kk_{\rm rg}}{\mu_{\rm g}} \left(-\frac{\partial P_{\rm g}}{\partial x} + g\rho_{\rm g} \right) \tag{3}$$

For countercurrent spontaneous imbibition, the total flow rate of water and air is zero. 30

$$v_{\rm w} + v_{\rm g} = 0 \tag{4}$$

The mobilities of water and gas can be expressed as $\lambda_{\rm w} = k_{\rm rw}/\mu_{\rm w}$ and $\lambda_{\rm g} = k_{\rm rg}/\mu_{\rm g}$, respectively.

Combining eqs 2-4, the water velocity is rewritten as

$$\nu_{\rm w} = \frac{k\lambda_{\rm w}\lambda_{\rm g}}{\lambda_{\rm w} + \lambda_{\rm g}} \left[\frac{\partial P_{\rm c}}{\partial x} + (\rho_{\rm w} - \rho_{\rm g})g \right]$$
 (5)

Substituting eq 5 into eq 1 yields

$$\frac{\partial}{\partial x} \left[\frac{k \lambda_{\rm w} \lambda_{\rm g}}{\lambda_{\rm w} + \lambda_{\rm g}} \frac{\partial P_{\rm c}}{\partial x} + \frac{k \lambda_{\rm w} \lambda_{\rm g}}{\lambda_{\rm w} + \lambda_{\rm g}} (\rho_{\rm w} - \rho_{\rm g}) g \right] = -\phi \frac{\partial S_{\rm w}}{\partial t} \tag{6}$$

The capillary pressure is $P_{\rm c} = P_{\rm g} - P_{\rm w}$ and a function of water saturation.

Equation 6 can be rewritten as

$$\frac{\partial}{\partial x} \left[D_{\text{sw}} \frac{\partial S_{\text{w}}}{\partial x} + G_{\text{sw}} (\rho_{\text{w}} - \rho_{\text{g}}) g \right] = -\phi \frac{\partial S_{\text{w}}}{\partial t}$$
(7)

 $D_{\rm sw}$ and $G_{\rm sw}$ denote nonlinear coefficients due to the capillary pressure and gravity.

$$D_{\rm sw} = \frac{k\lambda_{\rm w}\lambda_{\rm g}}{\lambda_{\rm w} + \lambda_{\rm g}} \frac{\mathrm{d}P_{\rm c}}{\mathrm{d}S_{\rm w}} \tag{8}$$

$$G_{\rm sw} = \frac{k\lambda_{\rm w}\lambda_{\rm g}}{\lambda_{\rm w} + \lambda_{\rm g}} \tag{9}$$

Equation 7 is the governing equation of OEO countercurrent spontaneous imbibition. If the gravity is negligible, eq 7 is simplified as

$$\frac{\partial}{\partial x} \left[D_{\rm sw} \frac{\partial S_{\rm w}}{\partial x} \right] = -\phi \frac{\partial S_{\rm w}}{\partial t} \tag{10}$$

The boundary conditions are given as

$$S_{w}(x=0,t) = S_{w,\max}$$
(11)

$$\left. \frac{\partial S_{\mathbf{w}}}{\partial x} \right|_{x=L} = 0 \tag{12}$$

The initial condition is expressed as

$$S_{w}(x, t = 0) = S_{wi} (13)$$

where $S_{\rm w,max}$ is the maximum water saturation, $S_{\rm wi}$ is the initial water saturation, and L is the length of the core plug.

Both numerical and analytical methods are capable of obtaining the solutions of eq 10 by matching model results with the specific experiments. However, there is no known exact solution of nonlinear eq 7, which considers the gravity effect. Thus, the finite difference method was used to obtain the numerical solutions. The time steps and grid spacing need to be small in order to minimize the error. In this paper, a time step of 2 s and a grid spacing of 0.1 mm were used to accurately capture the water imbibing into cores.

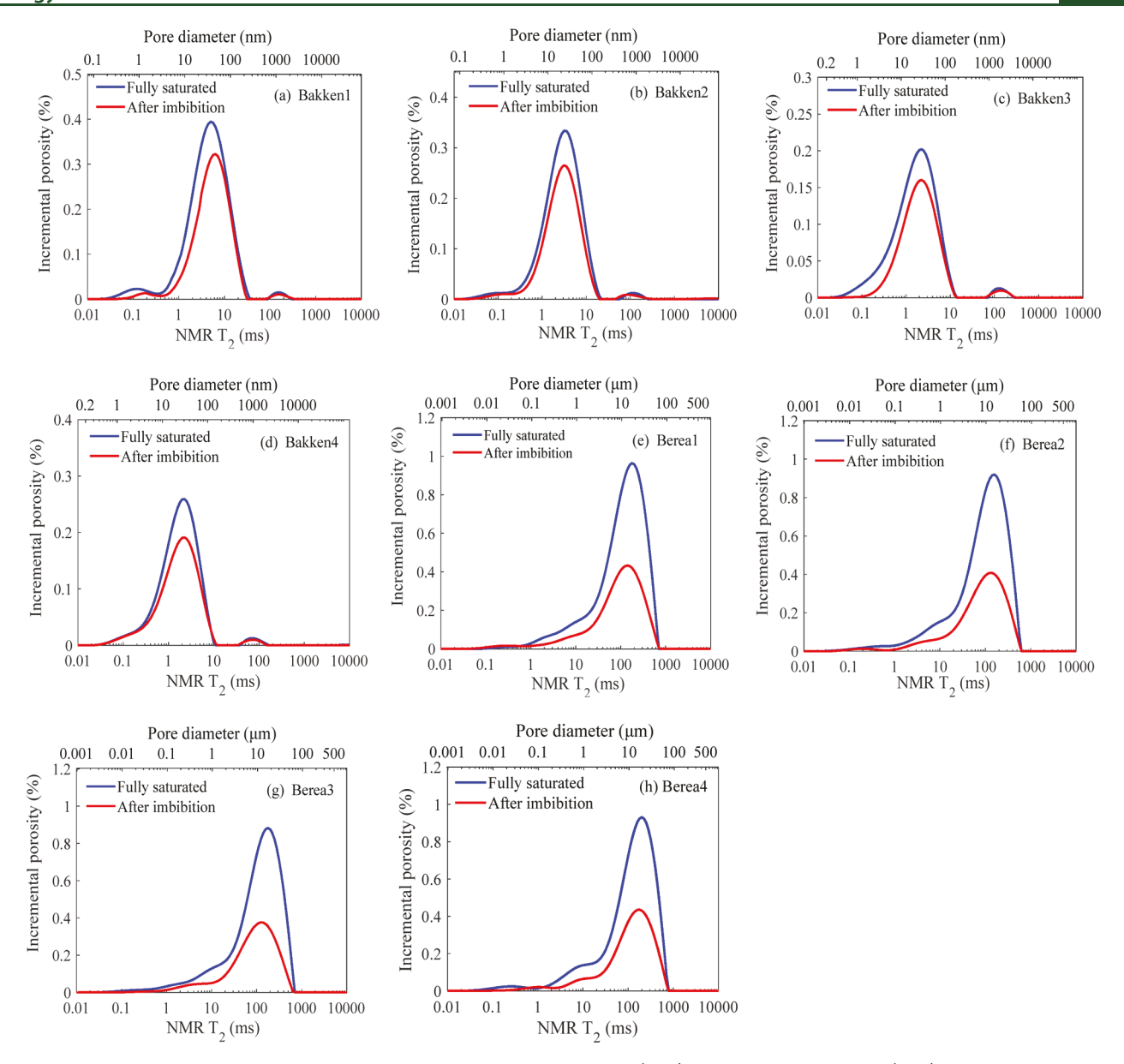


Figure 3. NMR T₂ and pore size distribution for Middle Bakken and Berea cores: (a-d) Middle Bakken samples; (e-h) Berea samples.

3.2. TEC Spontaneous Imbibition. Considering the experimental setup in this paper, the TEC countercurrent imbibition is a horizontal radial flow. The water conservation equation is expressed as

$$\frac{1}{r}\frac{\partial}{\partial r}(r\nu) = -\frac{\partial}{\partial t}(\phi S_{\rm w}) \tag{14}$$

Water-phase Darcy velocity is

$$v_{\rm w} = -\frac{kk_{\rm rw}}{\mu_{\rm w}} \frac{\partial P_{\rm w}}{\partial r} \tag{15}$$

Gas-phase (air) Darcy velocity is

$$v_{\rm g} = -\frac{kk_{\rm rg}}{\mu_{\rm g}} \frac{\partial P_{\rm g}}{\partial r} \tag{16}$$

Combining eqs 15 and 16 and eq 4, the water velocity is rewritten as

$$\nu_{\rm w} = \frac{k\lambda_{\rm w}\lambda_{\rm g}}{\lambda_{\rm w} + \lambda_{\rm g}} \frac{\partial P_{\rm c}}{\partial r} \tag{17}$$

Substituting eq 17 into eq 14 yields

$$\frac{1}{r}\frac{\partial}{\partial r}\left(rD_{\rm sw}\frac{\partial S_{\rm w}}{\partial r}\right) = -\phi\frac{\partial S_{\rm w}}{\partial t} \tag{18}$$

 $D_{\rm sw}$ is a nonlinear coefficient shown in eq 8. The boundary conditions are shown as

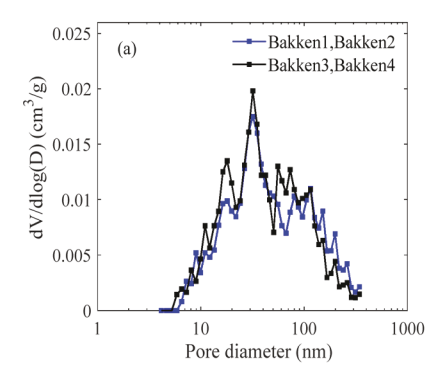
$$S_{\rm w}(r=r_{\rm e},\,t)=S_{\rm w,max} \tag{19}$$

$$\left. \frac{\partial S_{\mathbf{w}}}{\partial x} \right|_{r=0} = 0 \tag{20}$$

The initial condition is written as

$$S_{\rm w}(r, t=0) = S_{\rm wi}$$
 (21)

where $r_{\rm e}$ is the radius of the core plug.



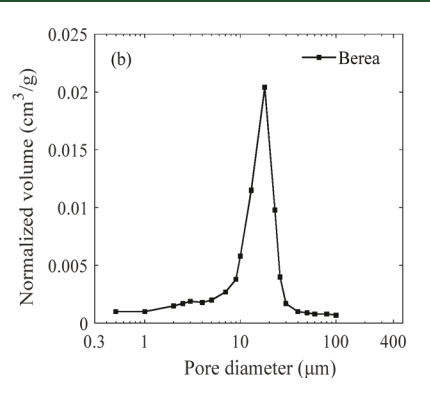


Figure 4. Pore size distribution of samples. (a) Middle Bakken samples from nitrogen adsorption; (b) Berea samples from mercury intrusion by Cardoso and Balaban.⁴⁷

Equation 18 is the governing equation of TEC countercurrent spontaneous imbibition. The finite difference method was used to obtain the numerical solutions. In order to capture the significant water saturation change at the imbibition front, it is necessary to define smaller grids at the core plug center. One method is to use nonuniform grids in that grid spacing increases exponentially and transforms cylindrical coordinates into Cartesian coordinates. In this paper, the space size is 0.1 mm in Cartesian coordinates, and the time step is 2 s.

3.3. Capillary Pressure and Relative Permeability. In this paper, a power law was used for the relative permeability curve. Other models such as Brooks—Corey and van Genuchten models could also be used. ^{29,31} However, the power law is a simple and most commonly used model in the modeling of spontaneous imbibition. ^{4,30} The power law could be written as

$$k_{\rm rw} = k_{\rm rw,max} \left(\frac{S_{\rm w} - S_{\rm wi}}{1 - S_{\rm wi} - S_{\rm gr}} \right)^{N_{k_{\rm rw}}}$$
 (22)

$$k_{\rm rg} = k_{\rm rg,max} \left(\frac{1 - S_{\rm w} - S_{\rm gr}}{1 - S_{\rm wi} - S_{\rm gr}} \right)^{N_{k_{\rm rg}}}$$
 (y23)

where $k_{\rm rw}$ is the water relative permeability, $k_{\rm rw,max}$ is the maximum water relative permeability, $S_{\rm w}$ is the water saturation, $S_{\rm wi}$ is the initial water saturation, $S_{\rm gr}$ is the residual gas saturation, $N_{k_{\rm rw}}$ is the water relative permeability exponent, $k_{\rm rg}$ is the gas relative permeability, $k_{\rm rg,max}$ is the maximum gas relative permeability, and $N_{k_{\rm rg}}$ is the gas relative permeability exponent.

A power law can be used to express the capillary pressure as shown in the following form³¹

$$P_{\rm c} = P_{\rm c,entry} \left(\frac{S_{\rm w} - S_{\rm wi}}{1 - S_{\rm wi} - S_{\rm gr}} \right)^{N_{P_{\rm c}}}$$
(24)

where $P_{\rm c,entry}$ is the entry capillary, $S_{\rm w}$ is the water saturation, $S_{\rm wi}$ is the initial water saturation, $S_{\rm gr}$ is the residual gas saturation, and $N_{P_{\rm c}}$ is the capillary pressure exponent.

This power law has an intrinsic flaw for the numerical method. At the imbibition front, $S_{\rm w}$ goes to $S_{\rm wi}$ and the capillary pressure goes to infinity. The power law does not make physical sense, and ${\rm d}P_{\rm c}/{\rm d}S_{\rm w}$ in eq 8 does not exist. Thus, we assume an exponential form for capillary pressure

$$P_{c} = P_{c,\text{max}} \exp \left[-\beta \left(\frac{S_{\text{w}} - S_{\text{wi}}}{1 - S_{\text{wi}} - S_{\text{gr}}} \right) \right]$$
(25)

where $P_{\rm c,max}$ is the maximum capillary pressure, $S_{\rm w}$ is the water saturation, $S_{\rm wi}$ is the initial water saturation, $S_{\rm gr}$ is the residual gas saturation, and β is a capillary pressure exponent.

The water saturation can be obtained by solving eqs 7, 10, and 18 numerically. The imbibed water volume can be calculated by integrating water saturation within the core. We adjusted the parameters $k_{\text{rw,max}}$, $N_{k_{\text{rw}}}$, $k_{\text{rg,max}}$, $N_{k_{\text{rg}}}$, $P_{\text{c,max}}$, and β to match between the numerical solutions and experimental results.

4. RESULTS AND DISCUSSION

4.1. NMR Pore Size and Fluid Distribution. An important application of NMR T_2 analysis is to transform NMR T_2 into pore size distribution (PSD). NMR T_2 responses can be converted to pore sizes using the following equation $^{40-43}$

$$\frac{1}{T_2} = \rho \left(\frac{S}{V}\right)_{\text{pore}} = \rho \frac{c}{R} \tag{26}$$

where ρ is the surface relaxivity, S/V is the ratio of pore surface area to pore volume, and R is the pore radius. c is 1, 2, and 3 for planar, cylindrical, and spherical pores, respectively. In this paper, pores are assumed to be cylindrical, and thus, c is 2. Equation 26 shows that the smaller the pore, the shorter the NMR relaxation time.

The pore size and T_2 distributions for Middle Bakken and Berea cores are presented in Figure 3. Two common features can be seen from the T_2 distribution. First, the signal of NMR T_2 shows a unimodal pattern. Second, the NMR T_2 signal after brine imbibition is much lower than when the core is fully brine-saturated.

In order to calculate NMR pore size distribution, the surface relaxivity should be calculated by comparing NMR T_2 distribution with PSD obtained from nitrogen adsorption or mercury intrusion. The peak of PSD measured from mercury intrusion is approximately proportional to the peak of T_2 distribution measured from NMR.⁴⁴ The equation is expressed as

$$R_{\text{peak}} = \rho c T_{2,\text{peak}} \tag{27}$$

where $R_{\rm peak}$ is the peak of PSD from mercury intrusion or nitrogen adsorption and $T_{\rm 2,peak}$ is the peak of NMR $T_{\rm 2}$ distribution.

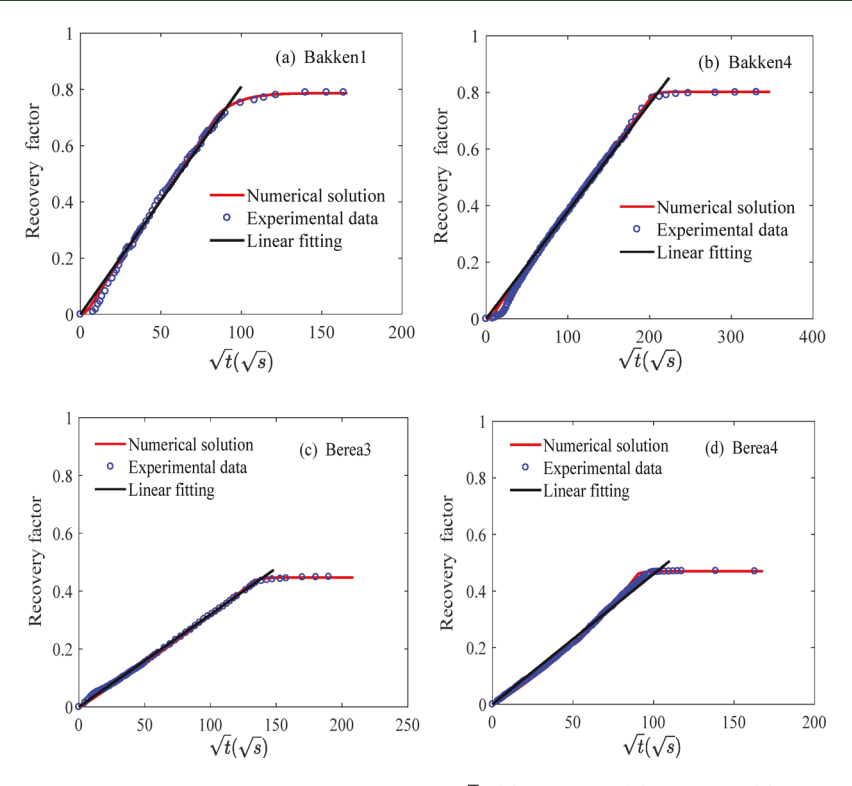


Figure 5. Recovery factors of OEO spontaneous imbibition as a function of \sqrt{t} : (a) Bakken1; (b) Bakken4; (c) Berea3; (d) Berea4.

Table 3. Parameters for Imbibition History Matching and Linear Fitting

samples	$S_{w,max}$	$k_{ m rw,max}$	$N_{k_{ m rw}}$	$k_{ m rg,max}$	$N_{k_{ m rg}}$	$P_{c,\max}$ (KPa)	β	$C(s^{-0.5})$	R^2
Bakken1	0.79	0.80	4	1	5	335	8.0	0.0081	0.989
Bakken4	0.80	0.40	8	1	5	460	2.5	0.0038	0.991
Berea3	0.45	0.70	6	1	4	10	2.1	0.0032	0.994
Berea4	0.47	0.68	8	1	4	14	4.3	0.0046	0.996
Bakken2	0.84	0.80	2	1	5	120	2.0	0.0131	0.895
Bakken3	0.78	0.40	8	1	5	370	2.4	0.0121	0.955
Berea1	0.47	0.70	2	1	4	20.5	2.0	0.0197	0.960
Berea2	0.47	0.67	2	1	4	19.5	2.0	0.0175	0.962

Nitrogen gas adsorption is able to detect micro- (<2 nm) to mesopores (2-50 nm), while mercury intrusion is capable of characterizing meso- to macropores (>50 nm). 45,46 The PSD of Berea outcrop samples is shown in Figure 4b reported by Cardoso and Balaban. 47 R_{peak} of the pore diameter distribution is 18 μ m. The surface relaxivity of Berea samples calculated from eq 27 is 23.7 μ m/s. However, the Middle Bakken is tight formation, and most of its pores are mesopores. Nitrogen adsorption is a common method to analyze tight formation PSD. 48-50 The PSD obtained from the nitrogen adsorption method can be used to calculate NMR surface relaxivity of tight rocks. 40,51 The PSDs of Bakken samples were measured using the nitrogen adsorption method (Figure 4a). Bakken1 and Bakken2 were obtained from the same depth and, Bakken3 and Bakken4 were obtained from another depth. The surface relaxivities of Bakken samples were calculated by matching $R_{\rm peak}$ from N₂ adsorption with $T_{\rm 2,peak}$ from NMR. The surface relaxivity is 3.4 µm/s for Bakken3 and Bakken4. The surface relaxivity is 1.8 μ m/s for Bakken1 and Bakken2. After the surface relaxivities were obtained, NMR transformed pore size was calculated using eq 27. Surface relaxivities of Berea and Middle Bakken cores are strikingly different. This significant difference can be attributed to NMR measurement parameters. NMR

settings such as spectrometer frequency, waiting time, and temperature have significant impacts on surface relaxivity. ^{52,53} The surface relaxivity differences between Middle Bakken samples are due to their mineralogical composition. The types and contents of paramagnetic minerals such as Fe-bearing chlorite, pyrite, and siderite have impacts on surface relaxivity. ⁵⁴ Samples Bakken3 and Bakken4 have larger surface relaxivities than Bakken1 and Bakken2 due to their high contents of paramagnetic minerals, namely, chlorite and pyrite, as shown in Table 1.

As presented in Figure 3, NMR pore diameters of Bakken cores range from 0.3 to 200 nm. Bakken samples are dominated by mesopores with only a small percentage of micropores and macropores. In addition, the pore diameter differences between Bakken samples are small. Those results are close to the Middle Bakken PSD from the mercury injection method by using unimodal PSD. 55 However, PSDs from transformed NMR show that Bakken samples exhibit a common feature in that a small content of water is present in fractures with width ranging from 0.6 to 2 μ m. This is because the Middle Bakken formation is naturally fractured. The nitrogen adsorption method is probably not capable of detecting those fractures because the samples used for nitrogen adsorption were crushed into 60–100 mesh

fragments. The crushing process probably destroyed the large fractures. For Bakken samples, NMR T_2 after imbibition indicates that water is capable of entering into the pores (1–200 nm) and fractures (0.6–2 μ m). Both Bakken and Berea samples show a common feature in that PSD curves are unimodal. The main difference is that Berea cores are dominated by macropores with diameters ranging from 0.1–60 μ m, which are much larger than the pores sizes of Bakken samples.

4.2. OEO Imbibition. The OEO imbibition is a linear imbibition. Considering the experimental setup, the gravity was considered in the mathematical model (eq 7). The recovery factor F can be calculated from the following equation

$$F = \frac{m}{(\rho_{\rm w} - \rho_{\rm g})V_p} \tag{28}$$

where *m* is the mass change of the core, $\rho_{\rm w}$ is brine density, $\rho_{\rm g}$ is air density, and $V_{\rm p}$ is pore volume

Experimental results, numerical solutions, and linear fittings are shown in Figure 5. By adjusting relative permeability and capillary pressure, the numerical model results were matched with the experimental data using the approaching method. The parameters for history matching, the slopes (*C*) and correlation coefficients (R^2) of linear fitting are presented in Table 3. Experimental results of all samples show a similar pattern. In all OEO experiments, imbibition curves have two stages: (1) At the early stage, the recovery factor increases rapidly and shows a linear relationship with the square root of time. However, samples Bakken1 and Bakken2 show a delay effect compared with numerical solutions; this phenomenon was possibly caused by the resistance of Bakken samples' oil-wet surface to wettability alteration by brine. (2) At the late stage, the recovery factor shows a sharp inflection point and quickly reaches the maximum value because the imbibition front reaches the bottom end of the core plug. The linear fitting of the recovery factor of OEO imbibition indicates a good linear relationship between the recovery factor and \sqrt{t} .

The ultimate recovery factors of Berea3 and Berea4 are 0.45 and 0.47, respectively (Figure 5). However, recovery factors of Bakken1 and Bakken4 are much higher, which are 0.79 and 0.8, respectively. Two factors may cause higher recovery factors in Bakken samples. First, the Middle Bakken formation is tight and naturally fractured.^{3,56} Pore structures of the Bakken samples are dominated by extremely small mesopores (Figure 3). The wetting phase is easy to be imbibed into smaller pores than into larger pores due to high capillary pressure.⁵⁰ This phenomenon can be seen from an interacting capillary model presented by Dong et al.⁵⁷ in that the wetting phase was imbibed into the smallest capillaries first and later into capillaries with increasing diameters. Based on this model, we presented a schematic diagram of countercurrent spontaneous imbibition with interacting capillaries as shown in Figure 6. The left end is the

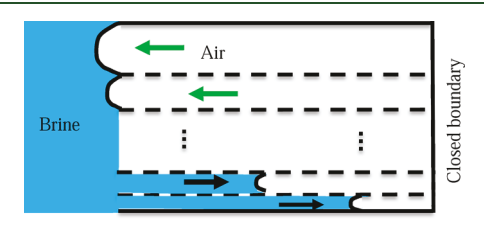


Figure 6. Schematic of interacting capillary bundle for countercurrent imbibition.

inlet, and the right end is the no flow boundary. Due to the capillary difference between large and small capillaries, the wetting phase imbibes into smaller capillaries and the non-wetting phase flows out of the larger capillaries. A large quantity of mesopores may cause high recovery factors of the Middle Bakken samples. Second, the non-wetting phase is much easier to be trapped in larger pores. Immiscible displacement experiments of a string of pore doublets conducted by Chatzis and Dullien⁵⁸ showed that the entrapment of the non-wetting phase is easy to occur in large pores, especially the bulge sandwiched between the two neck pores. This phenomenon can be explained by spreading and instability of bulk films ahead of the interface. This typical mechanism of non-wetting phase entrapment is presented in Figure 7. The flow in smaller pores is

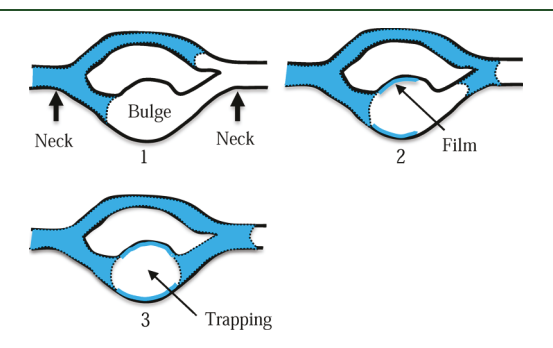


Figure 7. Illustration of trapping of non-wetting phase.

faster than the flow in larger pores. The non-wetting phase is much easier to be trapped in bulge than in smaller pores. Thus, a large quantity of large macropores in Berea samples (Figure 3) may cause low recovery factors of Berea cores.

Both the capillary and relative permeabilities can be obtained by matching mathematical models with experimental results. Considering the experimental setup, the mathematical model used is eq 7, which considers the gravity effect and is more accurate than the model in eq 10. The parameters $k_{\text{rw,max}}$, $N_{k_{\text{rw}}}$, $k_{\rm rg,max^{\prime}}\,N_{k_{\rm rg^{\prime}}}$ and $P_{\rm c,max}$ were obtained from the matching and are shown in Table 3. The capillary pressure and relative permeability curves are shown in Figures 8 and 9. The obtained maximal capillary pressures of Bakken1 and Bakken4 are approximately 335 and 460 KPa, respectively. Song and Yang⁵⁹ indicated that the maximal gas-liquid capillary pressure of tight Bakken formation is approximately 240-350 KPa, which is consistent with our results, whereas the maximal capillary pressure of Berea samples is much lower at about 10-14 KPa. This is similar to the result of Li et al., 28 which shows that the maximum capillary pressure of air-liquid for Berea cores is around 8 KPa.

4.3. Effect of Gravity on OEO Imbibition. The driving force of spontaneous imbibition is dominated by capillary forces. Gravity is usually neglected for spontaneous imbibition modeling. ^{11,28} In fact, gravity may impact the imbibition process and is one of the major concerns in the study of spontaneous imbibition. ^{1,60} In the experimental setup, brine can be vertically imbibed into cores through the top face. In such a case, gravity force contributes to the acceleration of the spontaneous imbibition process.

The recovery factor profiles of experiments and models considering and neglecting gravity are shown in Figure 10. In order to study the recovery in the absence of gravity, the cores were assumed to have the same capillary pressure and relative

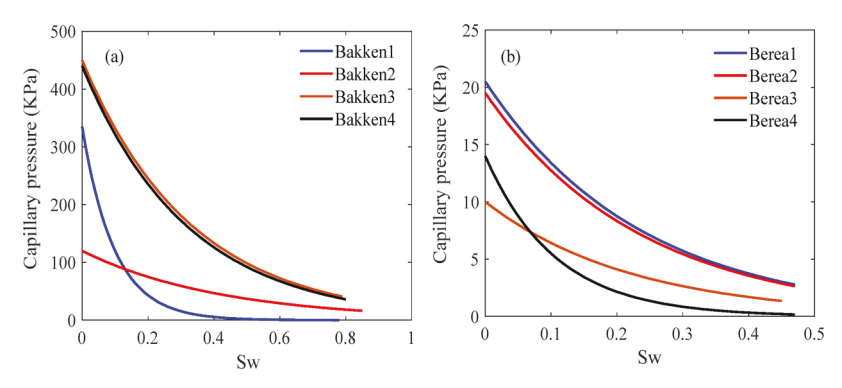


Figure 8. Capillary pressure curves of eight cores: (a) Bakken samples; (b) Berea samples.

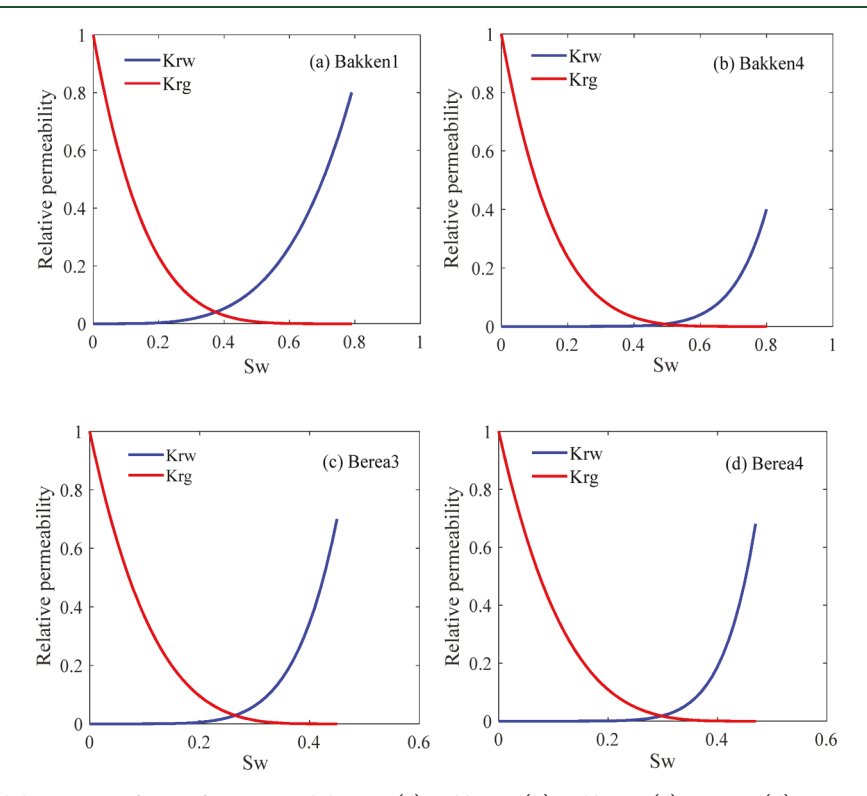


Figure 9. Relative permeability curves of cores for OEO imbibition: (a) Bakken1; (b) Bakken4; (c) Berea3; (d) Berea4.

permeability obtained from the history matching (Figures 8 and 9). For samples Bakken1 and Bakken4, recovery performances of the model with gravity are consistent with those of neglecting gravity. However, the recovery curves of samples Berea3 and Berea4 show a large deviation as the gravity is neglected. The deviation is small at the early stage and increases with time. The neglect of gravity force would cause underestimation of both recovery rate and ultimate recovery factor. As can be seen from Figure 10d, recovery of Berea4 reaches the equilibrium point at a time of 15000 s for the case of neglecting gravity force. However, the recovery of the case with the gravity force effect reaches the equilibrium point at a time of approximately 10000 s. In addition, the ultimate recovery factor in the absence of gravity is about 0.4, which is lower than the experimental recovery factor of 0.48. Those results confirm that the spontaneous imbibition of Berea cores is a capillary-gravity-dominated process. However, the imbibition processes of Bakken samples are dominated by capillary force. The capillary force of Bakken samples is much higher than that of Berea samples (Figure 8). By comparing capillary pressure and permeability data, it can be

further concluded that spontaneous imbibitions in tight rocks are dominated by the capillary force. However, spontaneous imbibitions in high-permeability rocks are controlled both by capillary force and gravity force. The gravity effect must be considered in the analysis of imbibition in high-permeability rocks.

4.4. TEC Imbibition. For TEC imbibition, the top and bottom faces of the Bakken2, Bakken3, Berea1, and Berea2 were sealed with epoxy resin. Thus, the TEC imbibition experiments for those cores are radial flow. Even though there have been many experimental studies on the TEC imbibition, ^{17,19,21} there are very few numerical studies focusing on this radial imbibition.

Experimental imbibition results, numerical solutions, and linear fittings for TEC imbibition are presented in Figure 11. At the early stage, the recovery factor increases rapidly and shows a linear relationship with \sqrt{t} . In the late stage, the recovery factor gradually reaches a plateau. The capillary pressure and relative permeability of Middle Bakken and Berea cores are presented in Figures 8 and 12, respectively. The Young—Laplace equation indicates that capillary pressure is proportional to the reciprocal

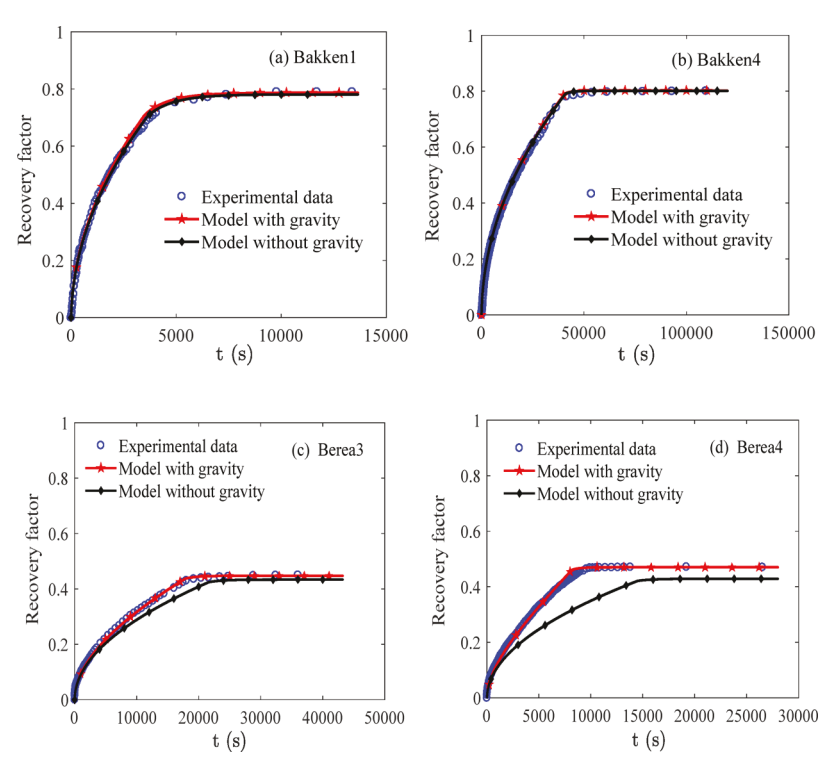


Figure 10. Recovery factors of experiments and models (with and without gravity) as a function of time: (a) Bakken1; (b) Bakken4; (c) Berea3; (d) Berea4.

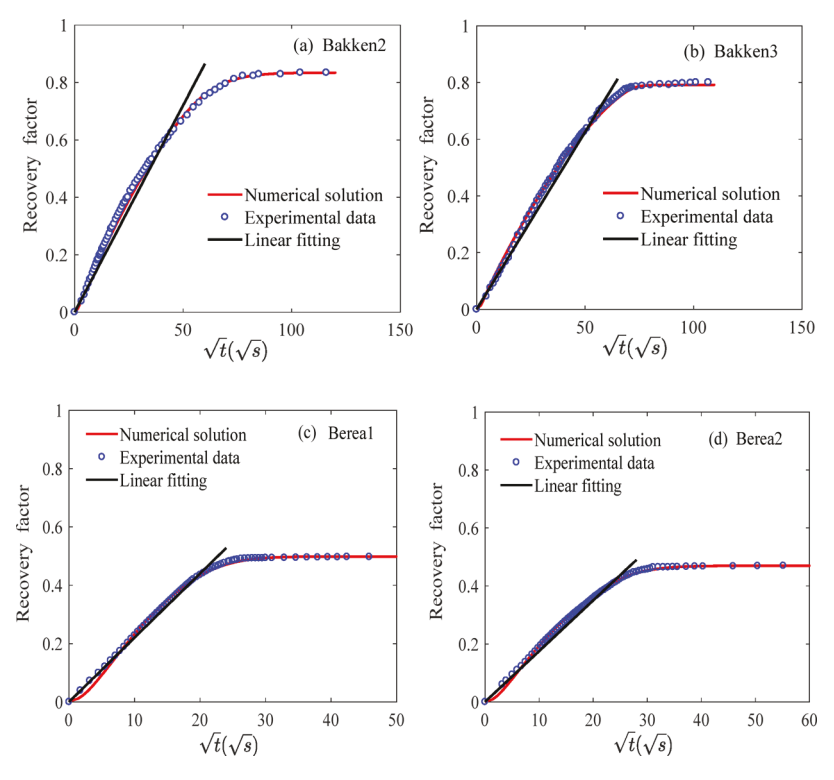


Figure 11. Recovery factors of cores for TEC imbibition as a function of \sqrt{t} : (a) Bakken1; (b) Bakken3; (c) Berea1; (d) Berea2.

of pore radius. The capillary pressures of Bakken samples are much higher than those of Berea samples. This is because the Bakken samples are tight rocks and the pore diameters are smaller than those of Berea samples (Figure 3). The parameters of numerical solutions and linear fitting are shown in Table 3. It is observed that correlation coefficients of TEC imbibition are

lower than those of OEC imbibition. In addition, experimental and numerical results indicate that the TEC imbibition has a poor relationship with \sqrt{t} at its late stage. Since diameters of Bakken and Berea samples are approximately the same, the slopes of linear fitting (Table 3) generally represent the imbibition rate. The slopes of Berea samples are higher than

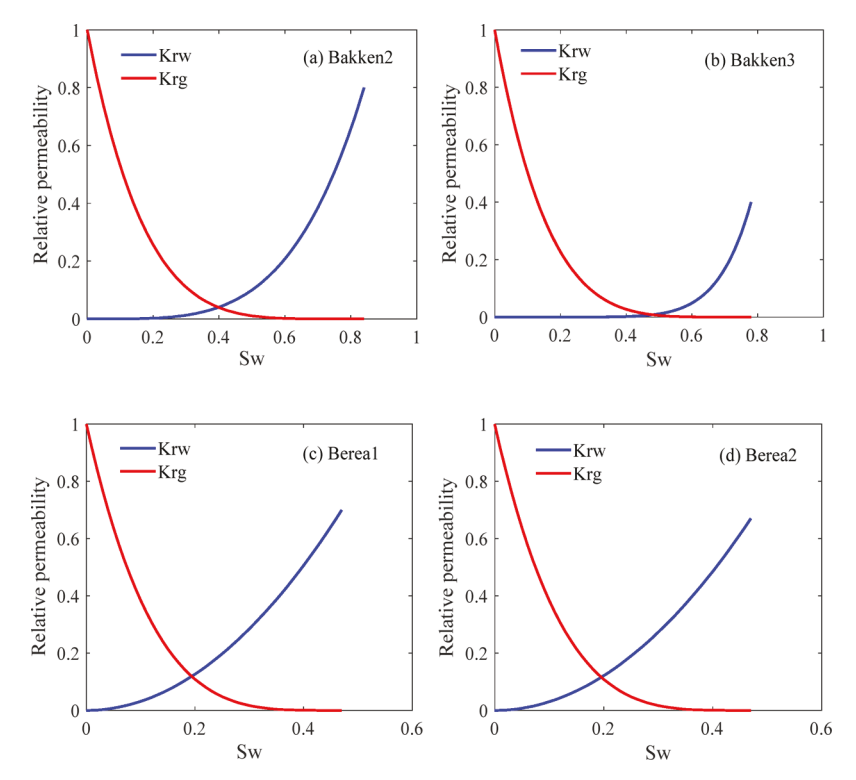


Figure 12. Relative permeability curves of cores for TEC imbibition: (a) Bakken2; (b) Bakken3; (c) Berea1; (d) Berea2.

those of Middle Bakken samples. Even though the capillary pressures of Berea samples are much lower than those of Bakken samples, imbibition rates of Berea samples are higher than those of Middle Bakken samples. Berea samples reach the peak recovery factor at 900 s, while the Bakken samples reach the peak at around 5000 s. This is because the permeabilities of the Berea cores are higher than those of Bakken samples. The imbibition rate is mainly dominated by the permeability rather than capillary pressure.

5. CONCLUSIONS

In this study, spontaneous imbibition experiments with OEO and TEC boundary conditions were performed on Bakken and Berea rocks and were analyzed by NMR. Mathematical models for those imbibition experiments were presented. New methods to obtain capillary pressure and relative permeability were proposed by matching mathematical models with imbibition experiments with different boundary conditions. Based on this study, the following conclusions were drawn:

- (1) NMR pore size distributions show that Bakken rocks have a large percentage of mesopores and a small amount of micropores, macropores, and fractures. Pore diameters range from 0.3 to 200 nm. Widths of the fractures range from 0.6 to 2 μ m. However, Berea rocks are dominated by macropores with diameters ranging from 0.07 to 70 μ m.
- (2) The recovery factor of OEO imbibition exhibits a linear relationship with \sqrt{t} . However, the recovery factor of TEC imbibition shows a good relationship with \sqrt{t} at its initial stage and a poor linear relationship with \sqrt{t} at its late stage.
- (3) For OEO and TEC spontaneous imbibition, the imbibition models are consistent with the experiments. The capillary and relative permeabilities were obtained from the matching. Recovery factors and capillary

- pressures of Bakken rocks are much higher than those of Berea rocks.
- (4) Gravity has insignificant effects on the recoveries of tight rocks. However, it has significant impacts on the recoveries of high-permeability rocks.

AUTHOR INFORMATION

Corresponding Author

*E-mail: hui.pu@und.edu.

ORCID ®

Hui Pu: 0000-0003-3074-3705

Notes

The authors declare no competing financial interest.

ACKNOWLEDGMENTS

The authors would like to thank the North Dakota Industrial Commission Oil and Gas Research Program (Contract No. G-041-081) and National Science Foundation (NSF1709160) for the financial support. We also thank North Dakota Geological Survey Wilson M. Laird Core and Sample Library for providing Bakken rock samples.

REFERENCES

- (1) Mirzaei-Paiaman, A. Analysis of counter-current spontaneous imbibition in presence of resistive gravity forces: Displacement characteristics and scaling. *J. Unconv. Oil. Gas. Resour* **2015**, *12*, 68–86.
- (2) Morrow, N. R.; Mason, G. Recovery of oil by spontaneous imbibition. *Curr. Opin. Colloid Interface Sci.* **2001**, *6*, 321–337.
- (3) Olatunji, K.; Zhang, J.; Wang, D. Effect of the rock dimension on surfactant imbibition rate in the Middle Member of Bakken: Creating a model for frac design. *J. Pet. Sci. Eng* **2018**, *169*, 416–420.
- (4) Wang, X.; Sheng, J. J. Spontaneous imbibition analysis in shale reservoirs based on pore network modeling. *J. Pet. Sci. Eng* **2018**, *169*, 663–672.

(5) Lai, F.; Li, Z.; Zhang, T.; Zhou, A.; Gong, B. Characteristics of microscopic pore structure and its influence on spontaneous imbibition of tight gas reservoir in the Ordos Basin, China. *J. Pet. Sci. Eng* **2019**, *172*, 23–31.

- (6) Yang, R.; Guo, X.; Yi, J.; Fang, Z.; Hu, Q.; He, S. Spontaneous Imbibition of Three Leading Shale Formations in the Middle Yangtze Platform, South China. *Energy Fuels* **2017**, *31*, 6903–6916.
- (7) Xu, M.; Binazadeh, M.; Zolfaghari, A.; Dehghanpour, H. Effects of Dissolved Oxygen on Water Imbibition in Gas Shales. *Energy Fuels* **2018**, 32, 4695–4704.
- (8) Wu, J.; Yu, J.; Wang, Z.; Fu, X.; Su, W. Experimental investigation on spontaneous imbibition of water in coal: Implications for methane desorption and diffusion. *Fuel* **2018**, *231*, 427–437.
- (9) Shen, J.; Zhao, J.; Qin, Y.; Shen, Y.; Wang, G. Water imbibition and drainage of high rank coals in Qinshui Basin, China. *Fuel* **2018**, *211*, 48–59
- (10) Foley, A. Y.; Nooruddin, H. A.; Blunt, M. J. The impact of capillary backpressure on spontaneous counter-current imbibition in porous media. *Adv. Water Resour.* **2017**, *107*, 405–420.
- (11) Alyafei, N.; Blunt, M. J. Estimation of relative permeability and capillary pressure from mass imbibition experiments. *Adv. Water Resour.* **2018**, *115*, 88–94.
- (12) Pooladi-Darvish, M.; Firoozabadi, A. Cocurrent and Counter-current Imbibition in a Water-Wet Matrix Block. *Soc. Pet. Eng. J.* **2000**, *5*, 3–11.
- (13) Chen, Q.; Gingras, M. K.; Balcom, B. J. A magnetic resonance study of pore filling processes during spontaneous imbibition in Berea sandstone. *J. Chem. Phys.* **2003**, *119*, 9609–9616.
- (14) Haugen, Å.; Fernø, M. A.; Mason, G.; Morrow, N. R. Capillary pressure and relative permeability estimated from a single spontaneous imbibition test. *J. Pet. Sci. Eng* **2014**, *115*, 66–77.
- (15) Xu, Z.; Cheng, L.; Cao, R.; Jia, P.; Wu, J. Simulation of countercurrent imbibition in single matrix and field scale using radical integral boundary element method. *J. Pet. Sci. Eng* **2017**, *156*, 125–133.
- (16) Mattax, C. C.; Kyte, J. R. Imbibition oil recovery from fractured, water-drive reservoir. Soc. Pet. Eng. J. 1962, 2, 177–84.
- (17) Yildiz, H. O.; Gokmen, M.; Cesur, Y. Effect of shape factor, characteristic length, and boundary conditions on spontaneous imbibition. *J. Pet. Sci. Eng* **2006**, *53*, 158–170.
- (18) Mason, G.; Fischer, H.; Morrow, N. R.; Ruth, D. W. Spontaneous Counter-Current Imbibition into Core Samples with All Faces Open. *Transp. Porous Media* **2009**, *78*, 199–216.
- (19) Lyu, C.; Ning, Z.; Chen, M.; Wang, Q. Experimental study of boundary condition effects on spontaneous imbibition in tight sandstones. *Fuel* **2019**, 235, 374–383.
- (20) Mason, G.; Morrow, N. R. Developments in spontaneous imbibition and possibilities for future work. *J. Pet. Sci. Eng* **2013**, *110*, 268–293.
- (21) Cheng, Z.; Wang, Q.; Ning, Z.; Li, M.; Lyu, C.; Huang, L.; Wu, X. Experimental Investigation of Countercurrent Spontaneous Imbibition in Tight Sandstone Using Nuclear Magnetic Resonance. *Energy Fuels* **2018**, 32, 6507–6517.
- (22) Standnes, D. C. Experimental Study of the Impact of Boundary Conditions on Oil Recovery by Co-Current and Counter-Current Spontaneous Imbibition. *Energy Fuels* **2004**, *18*, 271–282.
- (23) Graue, A.; Fernø, M. A. Water mixing during spontaneous imbibition at different boundary and wettability conditions. *J. Pet. Sci. Eng* **2011**, *78*, 586–595.
- (24) Wang, J.; Liu, H.; Qian, G.; Peng, Y.; Gao, Y. Investigations on spontaneous imbibition and the influencing factors in tight oil reservoirs. *Fuel* **2019**, *236*, 755–768.
- (25) Qin, T.; Javanbakht, G.; Goual, L.; Piri, M.; Towler, B. Microemulsion-enhanced displacement of oil in porous media containing carbonate cements. *Colloids Surf., A* **2017**, 530, 60–71.
- (26) Pan, B.; Li, Y.; Wang, H.; Jones, F.; Iglauer, S. CO₂ and CH₄ Wettabilities of Organic-Rich Shale. *Energy Fuels* **2018**, *32*, 1914–1922.
- (27) Qin, T.; Javanbakht, G.; Goual, L. Nanoscale Investigation of Surfactant-Enhanced Solubilization of Asphaltenes from Silicate-Rich Rocks. *Energy Fuels* **2019**, *33*, 3796–3807.

(28) Li, Y.; Ruth, D.; Mason, G.; Morrow, N. R. Pressures acting in counter-current spontaneous imbibition. *J. Pet. Sci. Eng* **2006**, *52*, 87–99.

- (29) Schmid, K. S.; Geiger, S.; Sorbie, K. S. Semianalytical solutions for cocurrent and countercurrent imbibition and dispersion of solutes in immiscible two-phase flow. *Water Resour. Res.* **2011**, *47*, W02550.
- (30) Alyafei, N.; Al-Menhali, A.; Blunt, M. J. Experimental and Analytical Investigation of Spontaneous Imbibition in Water-Wet Carbonates. *Transp. Porous Med* **2016**, *115*, 189–207.
- (31) Schmid, K. S.; Alyafei, N.; Geiger, S.; Blunt, M. J. Analytical Solutions for Spontaneous Imbibition: Fractional-Flow Theory and Experimental Analysis. *Soc. Pet. Eng. J.* **2016**, *21*, 2308–2316.
- (32) Prather, C. A.; Bray, J. M.; Seymour, J. D.; Codd, S. L. NMR study comparing capillary trapping in Berea sandstone of air, carbon dioxide, and supercritical carbon dioxide after imbibition of water. *Water Resour. Res.* **2016**, *52*, 713–724.
- (33) Song, Y.; Wang, S.; Yang, M.; Liu, W.; Zhao, J.; Wang, S. MRI measurements of CO2–CH4 hydrate formation and dissociation in porous media. *Fuel* **2015**, *140*, 126–135.
- (34) Liang, B.; Jiang, H.; Li, J.; Gong, C.; Jiang, R.; Qu, S.; Pei, Y.; Yang, H. Investigation of Oil Saturation Development behind Spontaneous Imbibition Front Using Nuclear Magnetic Resonance T_2 . Energy Fuels **2017**, 31, 473–481.
- (35) Lyu, C.; Ning, Z.; Wang, Q.; Chen, M. Application of NMR T_2 to Pore Size Distribution and Movable Fluid Distribution in Tight Sandstones. *Energy Fuels* **2018**, 32, 1395-1405.
- (36) Gao, H.; Li, H. Determination of movable fluid percentage and movable fluid porosity in ultra-low permeability sandstone using nuclear magnetic resonance (NMR) technique. *J. Pet. Sci. Eng* **2015**, 133, 258–267.
- (37) Zhang, H.-L.; Han, S.-J. Viscosity and Density of Water + Sodium Chloride + Potassium Chloride Solutions at 298.15 K. J. Chem. Eng. Data 1996, 41, 516–520.
- (38) Lemmon, E. W.; Jacobsen, R. T. Viscosity and Thermal Conductivity Equations for Nitrogen, Oxygen, Argon, and Air. *Int. J. Thermophys.* **2004**, *25*, 21–69.
- (39) Bush, I. NMR Studies of Enhanced Oil Recovery Core Floods and Core Analysis Protocols; Ph.D. Dissertation, University of Cambridge: Cambridge, U.K., 2018.
- (40) Yuan, Y.; Rezaee, R.; Verrall, M.; Hu, Si-Yu.; Zou, J.; Testmanti, N. Pore characterization and clay bound water assessment in shale with a combination of NMR and low-pressure nitrogen gas adsorption. *Int. J. Coal Geol.* **2018**, *194*, 11–21.
- (41) Dunn, K. J.; Bergman, D. J.; Latorraca, G. A. Nuclear magnetic resonance: petrophysical and logging applications; Pergamon Press: Amsterdam, 2002.
- (42) Yao, Y.; Liu, D.; Che, Y.; Tang, D.; Tang, S.; Huang, W. Petrophysical characterization of coals by low-field nuclear magnetic resonance (NMR). *Fuel* **2010**, *89*, 1371–1380.
- (43) Liu, Y.; Yao, Y.; Liu, D.; Zheng, S.; Sun, G.; Chang, Y. Shale pore size classification: An NMR fluid typing method. *Mar. Pet. Geol.* **2018**, *96*, 591–601.
- (44) Minagawa, H.; Nishikawa, Y.; Ikeda, I.; Miyazaki, K.; Takahara, N.; Sakamoto, Y.; Komai, T.; Narita, H. Characterization of sand sediment by pore size distribution and permeability using proton nuclear magnetic resonance measurement. *J. Geophys. Res.* **2008**, *113*, B07210.
- (45) Wang, J.; Dong, M.; Yang, Z.; Gong, H.; Li, Y. Investigation of Methane Desorption and Its Effect on the Gas Production Process from Shale: Experimental and Mathematical Study. *Energy Fuels* **2017**, *31*, 205–216.
- (46) Abell, A. B.; Willis, K. L.; Lange, D. A. Mercury Intrusion Porosimetry and Image Analysis of Cement-Based Materials. *J. Colloid Interface Sci.* 1999, 211, 39–44.
- (47) Cardoso, O. R.; Balaban, R. D. C. Comparative study between Botucatu and Berea sandstone properties. *J. South Am. Earth Sci.* **2015**, 62, 58–69.

(48) Wang, J.; Wang, B.; Li, Y.; Yang, Z.; Gong, H.; Dong, M. Measurement of dynamic adsorption—diffusion process of methane in shale. *Fuel* **2016**, *172*, 37–48.

- (49) Wang, J.; Yuan, Q.; Dong, M.; Cai, J.; Yu, L. Experimental investigation of gas mass transport and diffusion coefficients in porous media with nanopores. *Int. J. Heat Mass Transfer* **2017**, *115*, 566–579.
- (50) Sang, Q.; Zhang, S.; Li, Y.; Dong, M.; Bryant, S. Determination of organic and inorganic hydrocarbon saturations and effective porosities in shale using vacuum-imbibition method. *Int. J. Coal Geol.* **2018**, 200, 123–134.
- (51) Saidian, M.; Prasad, M. Effect of mineralogy on nuclear magnetic resonance surface relaxivity: a case study of Middle Bakken and Three Forks formations. *Fuel* **2015**, *161*, 197–206.
- (52) Xu, H.; Tang, D.; Zhao, J.; Li, S. A precise measurement method for shale porosity with low-field nuclear magnetic resonance: A case study of the Carboniferous—Permian strata in the Linxing area, eastern Ordos Basin, China. *Fuel* **2015**, *143*, 47–54.
- (53) Godefroy, S.; Fleury, M.; Deflandre, F.; Korb, J.-P. Temperature effect on NMR surface relaxation in rocks for well logging applications. *J. Phys. Chem. B* **2002**, *106*, 11183–11190.
- (54) Yuan, Y.; Rezaee, R. Impact of Paramagnetic Minerals on NMR-Converted Pore Size Distributions in Permian Carynginia Shales. *Energy Fuels* **2019**, 33, 2880–2887.
- (55) Cho, Y.; Eker, E.; Uzun, I.; Yin, X.; Kazemi, H. Rock characterization in unconventional reservoirs: A comparative study of Bakken, Eagle Ford, and Niobrara formations. In *SPE Low Perm Sympoium*; Denver, Colorado, May 5-6, 2016; Society of Petroleum Engineers: 2016; SPE-180239-MS.
- (56) Liu, K.; Ostadhassana, M.; Zou, J.; Gentzisc, T.; Rezaeeb, R.; Bubacha, B.; Carvajal-Ortizc, H. Multifractal analysis of gas adsorption isotherms for pore structure characterization of the Bakken Shale. *Fuel* **2018**, *219*, 296–311.
- (57) Dong, M.; Dullien, F. A. L.; Dai, L.; Li, D. Immiscible Displacement in the Interacting Capillary Bundle Model Part I. Development of Interacting Capillary Bundle Model. *Transp. Porous Med* **2005**, *59*, 1–18.
- (58) Chatzis, I.; Dullien, F. A. L. Dynamic Immiscible Displacement Mechanisms in Pore Doublets: Theory versus Experiment. *J. Colloid Interface Sci.* **1983**, *91*, 199–222.
- (59) Song, C.; Yang, D. Experimental and numerical evaluation of CO_2 huff-n-puff processes in Bakken formation. Fuel **2017**, 190, 145–162.
- (60) Lefebvre Du Prey, E. Gravity and Capillarity Effects on Imbibition in Porous Media. Soc. Pet. Eng. J. 1978, 18, 195–206.